International Journal of Heat and Fluid Flow 109 (2024) 109531

Contents lists available at ScienceDirect

International Journal of Heat and Fluid Flow

journal homepage: www.elsevier.com/locate/ijhff

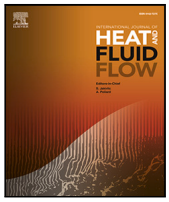

Anisotropy analysis of vortex breakdown states via direct numerical simulation

Jacopo Liberatori *, Mauro Valorani, Pietro Paolo Ciottoli

Department of Mechanical and Aerospace Engineering, Sapienza University of Rome, Via Eudossiana 18, 00184, Italy

ARTICLE INFO

Keywords:
Aerospace propulsion
Computational fluid dynamics
Direct numerical simulation
Vortex breakdown
Anisotropic turbulence
Swirling flows

ABSTRACT

Modeling highly swirling flows via second-moment closure approaches requires properly characterizing the turbulence dissipation tensor. In the present work, we investigate bubble-type and regular conical vortex breakdown states through direct numerical simulation. Consequently, we analyze the anisotropic features of the Reynolds stress and dissipation rate tensors using componentiality contours on the standard anisotropy maps. The anisotropy analysis reveals that the turbulence dissipation process exhibits a less significant departure from isotropic states than Reynolds stresses. Still, non-negligible anisotropy levels are envisaged around the breakdown-induced stagnation point, within the shear layer region, and at the top end of the central recirculation zone, highlighting the need for ad-hoc anisotropic modeling. Hence, we test a set of algebraic dissipation tensor models against the direct numerical simulation data, and we find out that blended formulations governed by the local turbulent Reynolds number can potentially identify the most anisotropic dissipation regions. However, this approach tends to revert to the classical isotropic treatment under the current formulation. Thus, improving both the blending function and the anisotropic contribution term is necessary. On the other hand, algebraic models directly relating the dissipation tensor to Reynolds stress anisotropies show worse agreement with the reference database, suggesting that the small-scale anisotropies instead descend from mean local flow field properties.

1. Introduction

Moderately to highly swirling flows can be encountered in various combustion processes due to the peculiar flow structures originating from the onset of the vortex breakdown (VB) phenomenon (Lucca-Negro and O'Doherty, 2001). Depending on the swirl level, two fundamental VB states are typically distinguished in the literature, namely, (i) the bubble-type breakdown and (ii) the regular conical breakdown. Under both circumstances, a significant enhancement of liquid fuel vaporization and fuel-oxidizer mixing is typically observed (Liberatori et al., 2024), and the onset of a reverse flow zone promotes the recirculation of hot-gas combustion products, thus enhancing aerodynamic flame stabilization (Syred and Beér, 1974).

Given their wide application range and beneficial effects on combustion, extensive experimental and high-fidelity numerical campaigns in the past decades provided thorough insights into VB-affected swirling flows' coherent structures and stability characteristics (Oberleithner et al., 2011). Fundamental results from those studies proved vital to developing computationally accessible Reynolds-averaged Navier–Stokes (RANS) closure models, which can be employed in large-scale computational fluid dynamics (CFD) and eventually offer a viable pathway toward computer-aided design optimization of combustion devices.

In this regard, second-moment closure (SMC) models discard Boussinesq's hypothesis and handle turbulent stresses' anisotropic features (Pope, 2000), constituting a valuable trade-off between predictive accuracy and computational burden (Blandino et al., 2024). Notably, SMC models address transport equations for the individual Reynolds stresses, $\langle u_i' u_j' \rangle$, where u_i is the ith component of the velocity field, the superscript denotes the fluctuating part, and angled brackets indicate an averaging operation:

$$\frac{D}{Dt}\langle u_i' u_j' \rangle = \Pi_{ij} + \mathcal{P}_{ij} - \varepsilon_{ij} + \mathcal{D}_{ij}. \tag{1}$$

In such transport equations, the substantial derivative D/Dt represents the mean-flow convection, $\Pi_{ij} = -\frac{1}{\rho}\langle u_i' \frac{\partial p'}{\partial x_j} + u_j' \frac{\partial p'}{\partial x_i} \rangle$ is the velocity-pressure-gradient correlation tensor, $\mathcal{P}_{ij} = -\langle u_i' u_k' \rangle \frac{\partial \langle u_j \rangle}{\partial x_k} - \langle u_j' u_k' \rangle \frac{\partial \langle u_i \rangle}{\partial x_k}$ is the production tensor, $\varepsilon_{ij} = 2\nu \langle \frac{\partial u_i'}{\partial x_k} \frac{\partial u_j'}{\partial x_k} \rangle$ is the turbulence dissipation tensor, and $\mathcal{D}_{ij} = \frac{\partial}{\partial x_k} \left(\nu \frac{\partial}{\partial x_k} \langle u_i' u_j' \rangle - \langle u_i' u_j' u_k' \rangle \right)$ indicates the contribution of viscous and turbulent diffusion, respectively. Here, ρ is

* Corresponding author.
E-mail address: jacopo.liberatori@uniroma1.it (J. Liberatori).

https://doi.org/10.1016/j.ijheatfluidflow.2024.109531
Received 5 March 2024; Received in revised form 2 July 2024; Accepted 2 August 2024
Available online 9 August 2024

the density, p is the pressure, ν is the kinematic viscosity. While $\mathcal{P}_{ij}$ and the viscous diffusion term are in closed form, ad-hoc modeling is required for the remaining terms. Specifically, the velocity-pressure-gradient correlation tensor is mostly modeled according to either the LRR model by Launder et al. (1975) or the SSG model by Speziale et al. (1991). Furthermore, a gradient-diffusion assumption is typically adopted to model the turbulent diffusion term (Pope, 2000). Concerning the turbulence dissipation tensor, the most commonly employed SMC approaches adopt the basic isotropic formulation, $\varepsilon_{ij} = \frac{2}{3}\varepsilon\delta_{ij}$, where ε – obtained by its own transport equation – is the average scalar dissipation rate of the turbulent kinetic energy, $k = \frac{1}{2}\langle u_i' u_i' \rangle$, and δ_{ij} is the Kronecker delta symbol. The latter formulation descends from Kolmogorov's hypothesis of local isotropy (Frisch, 1995), stating the tendency of small-scale turbulent structures to be isotropic regardless of the anisotropy level characterizing the large-scale energy-containing eddies in the limit of high Reynolds number (Saddoughi and Veeravalli, 1994), as a consequence of distinct scale separation between the energy spectrum and the dissipation spectrum.

Nonetheless, the idea of systematically approximating dissipative scales as locally isotropic was repeatedly argued from theory (Durbin and Speziale, 1991), numerical analyses (Yeung and Brasseur, 1991; Yeung et al., 1995), and experimental campaigns (Shen and Warhaft, 2000) under peculiar flow conditions and turbulence characteristics. In Durbin and Speziale (1991), Durbin and Speziale demonstrated that the local-isotropy hypothesis is erroneous in the presence of a sufficiently high strain rate, regardless of the Reynolds number levels. In Yeung and Brasseur (1991) and Yeung et al. (1995), Yeung et al. explored the development of small-scale anisotropy as a consequence of anisotropic forcing at the energy-containing scales via direct numerical simulation (DNS), suggesting that the outcome of this analysis should be applied even at high-Reynolds number limit. In Shen and Warhaft (2000), Shen and Warhaft highlighted the inadequacy of Kolmogorov's local isotropy postulate in a wind tunnel uniform shear flow at high laboratory Reynolds numbers. Concurrently, several studies demonstrated the distinctly anisotropic nature of turbulent motions at the dissipative scales, either within boundary layers (Antonia et al., 1994; Liu and Pletcher, 2008; Gerolymos and Vallet, 2016), stratified mixing layers (Smyth and Moum, 2000), corner separation regions of compressor cascades (Yan et al., 2019), or in the near-axis region of highly swirling flows undergoing VB (Yang et al., 2015), with the latter representing the object of study in the present work. In particular, Yang et al. (2015) pointed out via DNS study that large-scale vortex structures resulting from the onset of a VB phenomenon promote anisotropic turbulence dissipation. In contrast, isotropic dissipation features are confined to the peripheral region of swirling jets.

In this regard, improved models for the dissipation tensor were formulated in the past decades (Antonia et al., 1994; Liu and Pletcher, 2008; Rotta, 1951; Hanjalić and Launder, 1976; Hallbäck et al., 1996; Sjögren and Johansson, 2000; Hallbäck et al., 1990; Speziale and Gatski, 1997; So et al., 1999; Perot and Natu, 2004; Lai and So, 1990; Launder and Li, 1994; Oberlack, 1997). Still, none of those presented in the literature review above has emerged as a well-established, universal approach addressing complex industrial flows. In addition, concerning the anisotropy characteristics of swirling jets undergoing VB, limited databases are available (Yang et al., 2015), and anisotropic dissipation tensor models are yet untested against high-fidelity experimental or numerical data to the best of the authors' knowledge. Therefore, the objective of the present work is to provide a comprehensive anisotropy analysis of two prototypical swirling jets undergoing a bubble-type and a regular conical VB via DNS and to investigate a possible correlation between the anisotropic features of the Reynolds stresses and the dissipative scales. Moreover, we aim to test a collection of algebraic anisotropic dissipation tensor models against the DNS reference data, providing a guideline for the improved modeling of VB-affected swirling flows.

Hence, the paper is organized as follows. In Section 2, we introduce the two flow configurations investigated in the present study and the underlying numerical framework. Specifically, Section 2.1 illustrates the fundamental features of the swirling jets under examination, whereas Section 2.2 presents the governing equations and domain discretization. In Section 3, we provide an overview of the most commonly employed anisotropy maps, which are exploited to carry out the anisotropy analysis of the Reynolds stress and dissipation tensors in the remainder of the work by resorting to componentiality contours. Consequently, in Section 4, we first describe the anisotropic features of Reynolds stresses and dissipative turbulent scales under bubble-type and regular conical VB conditions, see Section 4.1. Moreover, in Section 4.2, in the first place, we review existing algebraic dissipation tensor models – see Section 4.2.1 – and then we test the performance of the isotropic model and a set of algebraic anisotropic dissipation tensor models, see Section 4.2.2. Lastly, in Section 5, we summarize the key results.

2. Numerical modeling

The present Section illustrates the two test configurations targeted throughout the research work, along with the governing equations and domain discretization.

2.1. Test case configuration

The present study addresses two prototypical single-phase swirling jets, replicating the flow conditions of the acetone/air spray swirling jets investigated in Liberatori et al. (2023). Specifically, we take into consideration two single-phase air swirling jets, at a temperature of 273.15 K, flowing out from an orifice of radius $R = 5 \cdot 10^{-3}$ m, and discharging in an open environment at atmospheric pressure. We impose the swirling motion on the inflow section by adopting a laminar Maxworthy inflow profile (Ruith et al., 2004), with no coflow outside the jet orifice. In this regard, in a cylindrical reference frame, the dimensionless form of the Maxworthy inflow profile returns the axial, tangential, and radial velocity components as:

$$u_z(\tilde{r}) = 1 - \frac{\alpha - 1}{2\alpha}\left[1 + \mathrm{erf}\left(\frac{\tilde{r} - 1}{\delta}\right)\right], \tag{2}$$

$$u_\theta(\tilde{r}) = \frac{S\tilde{r}}{2}\left[1 - \mathrm{erf}\left(\frac{\tilde{r} - 1}{\delta}\right)\right], \tag{3}$$

$$u_r(\tilde{r}) = 0. \tag{4}$$

where the velocity components are scaled by the centerline axial velocity, $u_{z,0}$, while the radial distance from the axis is scaled by R to provide the dimensionless radial distance, $\tilde{r}$. In Eq. (3), S denotes the swirl rate as the slope of the tangential velocity at the centerline, α is the core-to-coflow axial velocity ratio, expressing the ratio of the centerline axial velocity to the freestream velocity, and δ indicates the dimensionless shear layer thickness of the jet, i.e., the shear layer thickness scaled by R. In the present configurations, imposing no coflow on the inlet plane returns $\alpha = \infty$.

Two swirling regimes characterize the test case configurations, i.e., $S = 1.3$ for Case 1 and $S = 1.8$ for Case 2. On the other hand, the axial velocity profile remains unaltered, ensuring a bulk axial velocity $u_{z,b} = 8.1$ m/s and a centerline axial velocity $u_{z,0} = 9.25$ m/s, which results in a fixed bulk Reynolds number $Re_b = 2u_{z,b}R/\nu = 6000$. The latter corresponds to a configuration of technological interest regarding swirl-stabilized burners (Choi and Do, 2018; Jalalatian et al., 2019). Furthermore, the dimensionless shear layer thickness equals $\delta = 0.25$ for both configurations, with the velocity components provided by Eqs. (2)–(4) being transformed from the cylindrical to the Cartesian coordinate system during pre-processing.

Lastly, Fig. 1(a) illustrates a three-dimensional view of the test case geometry, along with a qualitative representation of coherent vortex structures arising under Case 2 flow conditions by Q-criterion isosurfaces.

2.2. Governing equations and domain discretization

We carry out the DNS computations within the OpenFOAM CFD environment through the pressure-based *rhoPimpleFoam* solver, leveraging a second-order discretization accuracy for the advective and diffusive terms. The full set of governing equations in the Cartesian coordinate system follows:

$$\frac{\partial \rho}{\partial t} + \frac{\partial (\rho u_j)}{\partial x_j} = 0, \tag{5}$$

$$\frac{\partial (\rho u_i)}{\partial t} + \frac{\partial}{\partial x_j}\left[\rho u_i u_j + p\delta_{ij} - \tau_{ij}\right] = 0, \tag{6}$$

$$\frac{\partial \rho h_t}{\partial t} + \frac{\partial}{\partial x_j}\left[\rho h_t u_j + q_j\right] = \frac{\partial p}{\partial t}, \tag{7}$$

$$p = \rho R_m T, \tag{8}$$

where $\boldsymbol{\tau}$ is the viscous stress tensor, h_t is the total enthalpy, given by the sum of sensible enthalpy and kinetic energy, $\boldsymbol{q}$ is the heat transfer rate, T is the temperature, and R_m is the specific gas constant of air. Moreover, the Prandtl number is set to 0.71. Notably, during the post-processing of the DNS datasets provided by Case 1 and Case 2, we transform vector and second-order tensor fields from the Cartesian to the cylindrical coordinate system.

As shown in Fig. 1(a), the computational domain consists of a cylinder with a diameter $D_{dom} = 16R$ and a longitudinal extension $L_{dom} = 25R$. We discretize the computational domain by 45M grid points leveraging the *blockMesh* utility provided within the OpenFOAM CFD toolbox and adopting $N_x \times N_y \times N_z = 425 \times 425 \times 450$ cells in the Cartesian reference frame with ad-hoc mesh grading, see Fig. 1(b). The mesh resolution is twice the Kolmogorov's length scale, $\eta_K = (\nu^3/\epsilon)^{0.25}$, on average for both Case 1 and Case 2. In this regard, the characteristic grid element size is taken as the cubic root of each cell's volume. Further details about the mesh resolution across the entire computational domain can be found in Liberatori et al. (2023).

The initial velocity field corresponds to quiescent conditions, while we set the pressure and temperature to 101325 Pa and 273.15 K uniformly over the computational domain, respectively. Moreover, we summarize the adopted boundary conditions in Table 1. We adequately select the physical time-step, i.e., $\Delta t = 6.25 \cdot 10^{-7}$ s and $\Delta t = 4.5 \cdot 10^{-7}$s for Case 1 and Case 2, respectively, so that the maximum Courant number does not exceed 0.2 within the computational domain under both test case configurations. Nonetheless, defining a characteristic flow-through time (FTT) as $FTT = L_{dom}/u_{z,b}$, we observe the flow developing into a statistically steady state after 20 flow-through times. Thereafter, we average the selected quantities of interest over 30 flow-through times. In this regard, in the remainder of the text, mean quantities extracted from the DNS computations should be intended as the result of an averaging operation taken on both time and the tangential direction, θ.

Lastly, although this is not thoroughly discussed in the present research study for the sake of brevity, we preliminarily validate the OpenFOAM-based DNS solver against direct numerical simulations of swirling flows undergoing bubble-type and regular conical VB states (Liberatori et al., 2024), carried out by adopting a cylindrical staggered mesh and leveraging central finite differences schemes and time integration by a low-storage, third-order, Runge–Kutta scheme (Dalla Barba and Picano, 2018; Ciottoli et al., 2021).

3. Anisotropy characterization and tensor componentiality

The anisotropic features of second-order symmetric tensors as the Reynolds stress and turbulence dissipation tensors can be isolated by introducing the anisotropy tensors, b_{ij} and d_{ij}, which exclusively retain the deviatoric part. Notably, $b_{ij} = \frac{\langle u_i' u_j' \rangle}{2k} - \frac{\delta_{ij}}{3}$ and $d_{ij} = \frac{\epsilon_{ij}}{2\epsilon} - \frac{\delta_{ij}}{3}$ are the Reynolds stress and turbulence dissipation anisotropy tensors, respectively (Lumley and Newman, 1977). Moreover, different anisotropy maps were developed (Lumley and Newman, 1977; Banerjee et al., 2007) to characterize turbulence-related tensor characteristics and componentiality comprehensively.

Table 1
Description of the boundary conditions adopted in the direct numerical simulations of Case 1 and Case 2. Here, p_0 indicates the total pressure, while ZG denotes a zero-gradient boundary condition.

Boundary	Conditions
Inlet	Pressure: ZG, Temperature: $T = 273.15$ K, Velocity: Eqs. (2)–(4)
Coflow	Pressure: $p_0 = 101\,325$ Pa, Temperature: ZG, Velocity: ZG
Ambient	Pressure: $p_0 = 101\,325$ Pa, Temperature: ZG, Velocity: ZG
Outlet	Pressure: ZG, Temperature: ZG, Velocity: ZG

In the first place, Lumley and Newman (1977) proposed the anisotropy invariant map or Lumley triangle, illustrated in Fig. 2(a), i.e., a confined region, defined upon the second and third principal tensor invariants, e.g., $II_b = b_{ij}b_{ji}$ and $III_b = b_{ij}b_{jk}b_{ki}$ for the Reynolds-stress anisotropy, which contains any realizable turbulence state. The principal invariants of the dissipation anisotropy tensor, II_d and III_d, are defined similarly. Notably, three limiting turbulence states determine the corners of the Lumley triangle: (i) 3C, or three-component isotropic turbulence, with anisotropy tensor eigenvalues $\lambda_1 = \lambda_2 = \lambda_3 = 0$; (ii) 2C, or two-component axisymmetric turbulence, with anisotropy tensor eigenvalues $\lambda_1 = \lambda_2 = 1/6$ and $\lambda_3 = -1/3$; (iii) 1C, or one-component turbulence, with anisotropy tensor eigenvalues $\lambda_1 = 2/3$ and $\lambda_2 = \lambda_3 = -1/3$. Furthermore, the boundaries connecting the fundamental limiting states designate specific turbulence characteristics, namely: (i) 1C-2C, or two-component limit, which distinctively describes near-wall turbulence (Antonia et al., 1994); (ii) 1C-3C, or axisymmetric expansion, which corresponds to rod-like (oblate spheroid) turbulence; (iii) 2C-3C, or axisymmetric contraction, which corresponds to pancake-like (prolate spheroid) turbulence. Lastly, a plane-strain region, identified through a dashed line in Fig. 2(a), constitutes the locus of points where one anisotropy eigenvalue is zero. Specifically, from the standpoint of the turbulent stresses, along the plane-strain limit, the mean momentum exchange due to fluctuating velocities exclusively acts over a plane. At the same time, perfectly isotropic fluctuations affect the remaining principal direction and give a vanishing contribution. Nonetheless, exploiting the eigenvalue decomposition allows to visualize ellipsoid-like glyphs (Simonsen and Krogstad, 2005), as shown in Fig. 2(a), which provide valuable information on the componentiality of any turbulence-related tensor.

However, the non-linear dependence of the principal invariants on the eigenvalues of the anisotropy tensors is known to induce a visual bias in the Lumley triangle about the turbulence states, which are primarily driven toward the axisymmetric expansion boundary (Emory and Iaccarino, 2014). To address this issue, Banerjee et al. (2007) introduced a barycentric map in the shape of an equilateral triangle, as shown in Fig. 2(b), which features a linear dependence on the anisotropy tensor eigenvalues. Notably, the three fundamental limiting states define the corners of the barycentric map, and the interconnecting boundaries still designate the two-component, axisymmetric expansion and axisymmetric contraction limits. Subsequently, any intermediate turbulence state can be obtained as a convex combination of the limiting states through a set of weight coefficients $\{C_{1C}, C_{2C}, C_{3C}\}$, namely as:

$$\hat{x} = C_{1C}x_{1C} + C_{2C}x_{2C} + C_{3C}x_{3C} \qquad \hat{y} = C_{1C}y_{1C} + C_{2C}y_{2C} + C_{3C}y_{3C}, \tag{9}$$

where $\hat{x}$ and $\hat{y}$ denote the barycentric coordinates of the turbulence state under consideration, whereas x_{iC} and y_{iC} indicate the barycentric coordinates of the ith limiting state. The linear nature of the barycentric map is reflected in the fact that the weight coefficients are linear functions of the anisotropy tensor eigenvalues, i.e., $C_{1C} = \lambda_1 - \lambda_2$,

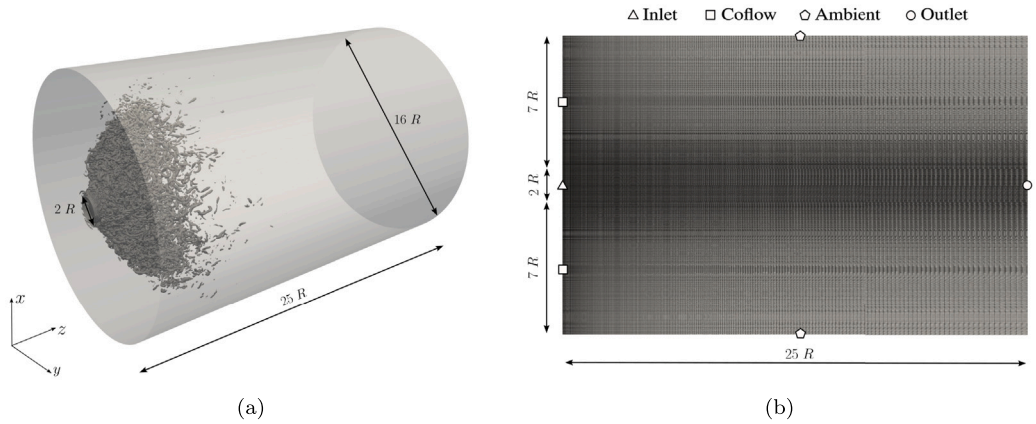

Fig. 1. Computational domain for the direct numerical simulations of Case 1 and Case 2: (a) three-dimensional visualization of the test case geometry along with relevant geometrical dimensions and representative Q-criterion isosurfaces, $Q = 4.0 \times 10^6$, for Case 2, (b) longitudinal view of the discretized computational domain, displaying boundary sections. Note that R denotes the jet orifice radius, $R = 5 \cdot 10^{-3}$ m.

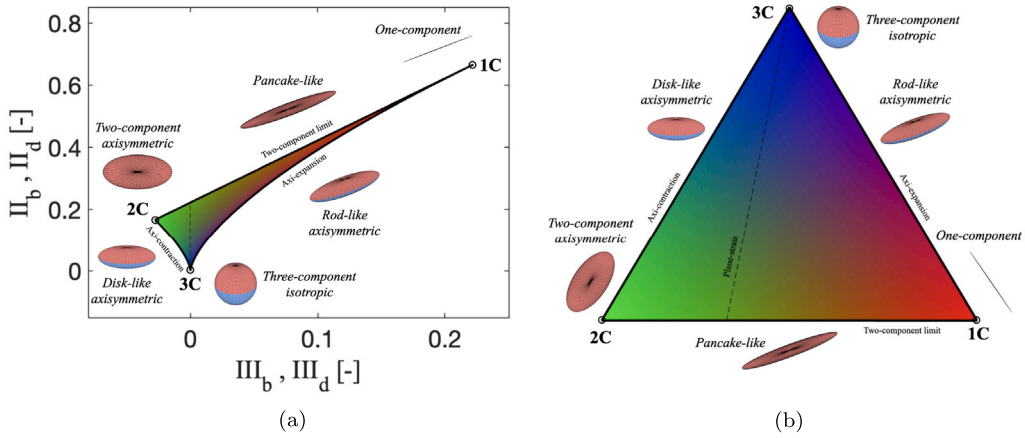

Fig. 2. Turbulence anisotropy maps, colored with componentiality contours: (a) Lumley triangle (Lumley and Newman, 1977), (b) barycentric map (Banerjee et al., 2007). The limiting states (1C, 2C, 3C), the boundaries of the maps, and the plane-strain limit (dashed line) are labeled, and ellipsoid-like glyphs represent the corresponding shape of Reynolds stress and turbulence dissipation tensors. (For interpretation of the references to color in this figure legend, the reader is referred to the web version of this article.)

$C_{2C} = 2(\lambda_2 - \lambda_3)$, and $C_{1C} = 3\lambda_3 + 1$, where $\lambda = (\lambda_1, \lambda_2, \lambda_3)$ designates the anisotropy tensor eigenvalues in descending order.

Regardless of the linear or non-linear dependency on the anisotropy tensor eigenvalues, the possibility of visualizing extensive amounts of data on standard anisotropy maps presented above is limited. Indeed, one shortcoming of the Lumley triangle and the barycentric map is the lack of a connection between the turbulence states depicted within the map region and their spatial distribution within the turbulent flow field under examination. In other words, information about the anisotropic nature of turbulence-related tensors is extracted from the flow spatial domain and graphically represented in the anisotropy maps, thus denying the opportunity to simultaneously characterize any region's anisotropic features in the flow configuration of interest. Based on these considerations, Emory and Iaccarino (2014) proposed a novel visualization technique, which provides anisotropy maps equipped with componentiality contours, as illustrated in Fig. 2 for both the Lumley triangle and the barycentric map. In particular, a red-green-blue color system is adopted so that the limiting turbulence states are colored in red (1C), green (2C), and blue (3C). In contrast, any other intermediate state is represented by combining the red-green-blue color channels through the weight coefficients $\{C_{1C}, C_{2C}, C_{3C}\}$. This way, the information about the anisotropic characteristics of turbulence-related tensors may be directly transferred from the anisotropy maps to the spatial domain of the turbulent flow field taken into account, providing valuable information about those flow regions mostly affected by anisotropic turbulence behavior and guiding ad-hoc improvement of the turbulence modeling. Hence, in the following, we will exploit this kind of visualization strategy to carry out a thorough anisotropy analysis of Reynolds stresses and dissipative scales for Case 1 and Case 2.

4. Results and discussion

Based on the theoretical framework illustrated in Section 3, we first analyze the anisotropic features of the Reynolds stress and turbulent dissipation tensors arising under Case 1 and 2, i.e., under bubble-type and regular conical VB conditions, see Section 4.1. Then, we investigate the performance of the isotropic formulation and a set of algebraic anisotropic dissipation tensor models available in the open literature against the reference DNS database, see Section 4.2.

4.1. Reynolds stresses and turbulence dissipation anisotropy analysis

In the first place, Fig. 3 illustrates the mean velocity field characterizing Case 1 (left panel) and Case 2 (right panel). As already stated, both configurations exhibit the establishment of a VB phenomenology, which results in the onset of a central recirculation zone (CRZ), evidenced by Fig. 3(a), showing the mean axial velocity field. Notably, the moderate swirling level of Case 1 promotes the onset of a bubble-type VB, with a stagnation point placed in proximity of $z/R \approx 1.5$,

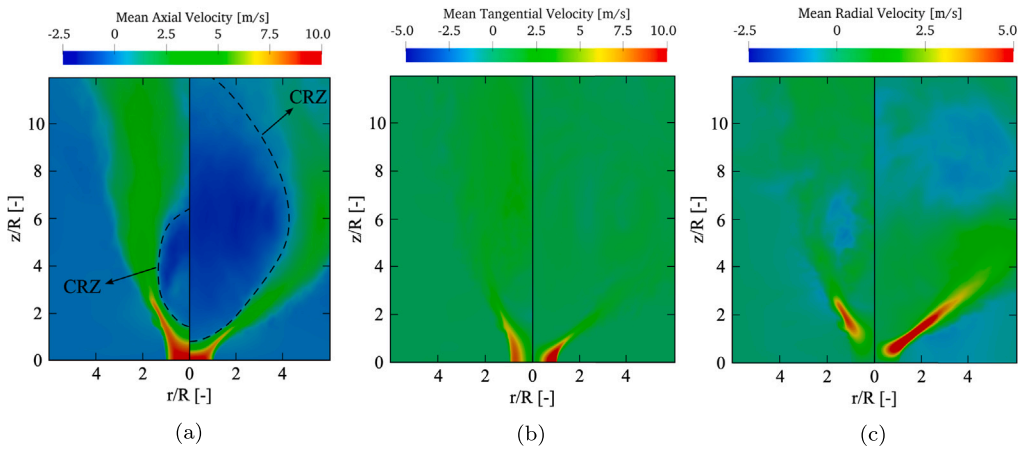

Fig. 3. Mean velocity field contour maps for Case 1 (left) and Case 2 (right): (a) axial velocity, with black contour lines denoting the VB-induced central recirculation zone (CRZ), (b) tangential velocity, (c) radial velocity.

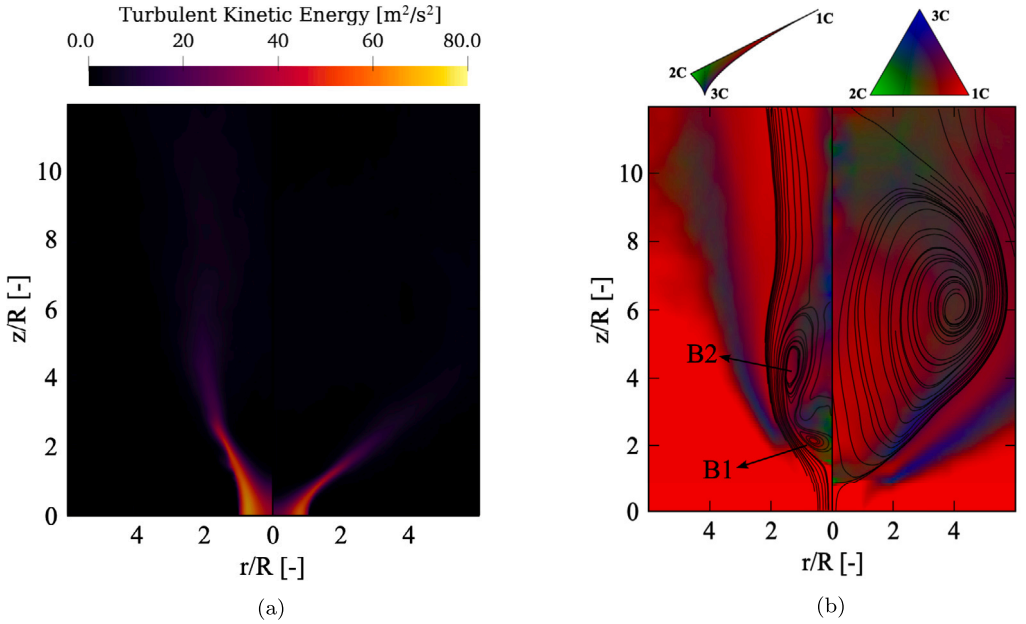

Fig. 4. Reynolds stress tensor characteristics for Case 1 (left) and Case 2 (right): (a) mean turbulent kinetic energy, (b) componentiality of the Reynolds stress tensor, overlapped with mean velocity field streamlines (solid lines). Here, B1 and B2 denote the smaller and larger recirculation bubbles arising under bubble-type VB conditions.

a CRZ extending up to $z/R \approx 6$, and a limited radial jet spreading, see Fig. 3(c). The decay of tangential momentum is very pronounced, as shown in Fig. 3(b), while the axial velocity distribution reported in Fig. 3(a) highlights the presence of a recovery region, with an expanded vortex core, beyond the CRZ, where a wake-like velocity profile establishes. On the contrary, the high swirling intensity characterizing Case 2 results in a regular conical VB state, which features the upstream motion of the stagnation point compared with Case 1, namely, at $z/R \approx 1$, and an enlargement of the CRZ. Furthermore, this is accompanied by a largely enhanced jet spreading and a consequent faster decay of the tangential momentum. In contrast, the presence of a recovery region with significant axial momentum levels is less evident.

In Fig. 4(a), a contour map of the mean turbulent kinetic energy, k, is reported for Case 1 (left panel) and Case 2 (right panel). Under both swirl regimes, a fast decay of the turbulent kinetic energy along the jet evolution is observed, whereas considerably low values characterize the CRZ. To characterize Reynolds stress anisotropy, Fig. 4(b) illustrates a componentiality contour map relative to the Reynolds stress tensor – following the color notation presented in Fig. 2 – overlapped with the mean velocity field streamlines for Case 1 (left panel) and Case 2 (right panel). Concerning the moderate-swirl condition, it is worth noting that the CRZ features a two-cell structure (Meunier and Hourigan, 2013), which results in the onset of two toroidal recirculation bubbles, denoted as B1 and B2 in Fig. 4(b). The componentiality contour map reveals an almost isotropic nature of Reynolds stresses along the outer shear layer (OSL) from $z/R \approx 2$ on, with an anisotropy level slightly increasing further downstream. On the contrary, the jet evolution is characterized by a one-component nature of Reynolds stresses. Perfectly two-component behavior of turbulent stresses is observed at the lower end of the CRZ, i.e., at $z/R \approx 2$, just upstream of the smaller recirculation bubble (B1), which in turn exhibits a one-component nature of the Reynolds stresses, similar to the larger recirculation bubble (B2). In the region between the two recirculation bubbles, i.e., around $z/R \approx 3$, the Reynolds stress anisotropy states shift toward the axisymmetric contraction (2C-3C) boundary of the anisotropy maps. Lastly, the near-axis region downstream of the CRZ, beyond $z/R \approx 6$, is characterized by an almost vanishing anisotropy degree of the Reynolds stresses. Concerning Case 2, the regular conical VB gives rise to a single recirculation bubble. Nearly perfect isotropy of the turbulent stresses can be envisaged in the initial portion of the inner shear layer (ISL) and the OSL. At the

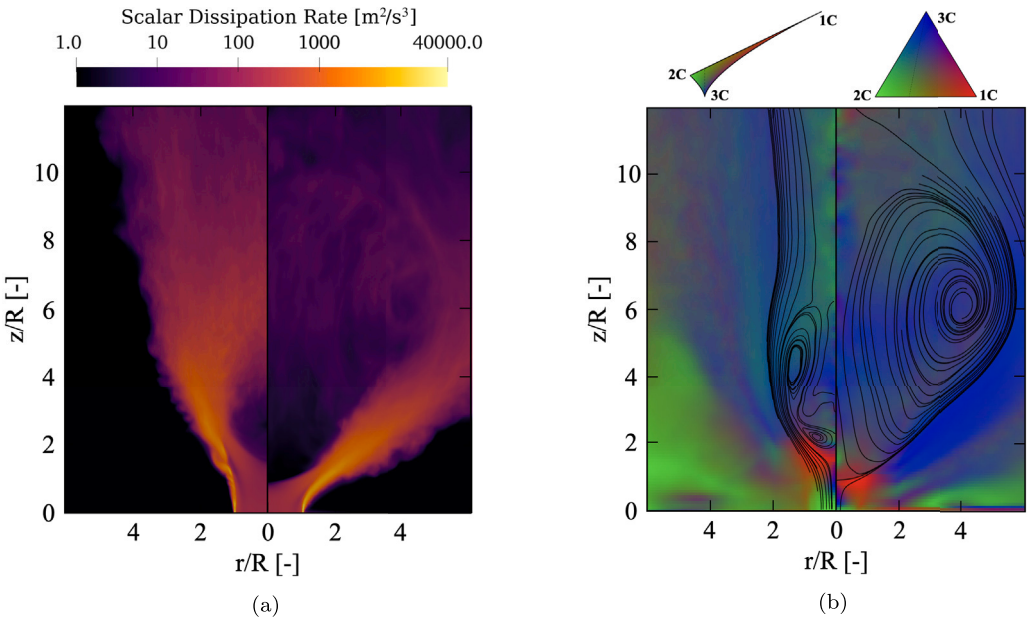

Fig. 5. Turbulence dissipation tensor characteristics for Case 1 (left) and Case 2 (right): (a) mean scalar dissipation rate of the turbulent kinetic energy, (b) componentiality of the turbulence dissipation tensor, overlapped with mean velocity field streamlines (solid lines). Note that a logarithmic scale is used for the contour map of the mean scalar dissipation rate.

same time, a two-component nature is still evident at the bottom of the CRZ. Lastly, Reynolds stresses again demonstrate a tendency toward the axisymmetric contraction limit downstream of the latter.

Fig. 5 provides analogous information about the nature of the dissipative turbulent motions. From Fig. 5(a), it is evident how the average scalar dissipation rate of the turbulent kinetic energy is mainly concentrated along the OSL and main jet regions, while the CRZ exhibits lower values of ε. Under Case 1 conditions, as shown in Fig. 5(b), a perfectly one-component nature of the turbulence dissipation process is observed in the proximity of the stagnation point, approximately between $z/R \approx 1.5$ and $z/R \approx 2$. At the same time, lower anisotropy levels are envisaged elsewhere. Specifically, in the peripheral region of the jet, the turbulence dissipation tensor oscillates between the 2C and 3C limiting states. Within the smaller recirculation bubble (B1), small-scale anisotropy states move toward the axisymmetric expansion (1C-3C) limit, while the larger recirculation bubble (B2) features a turbulence dissipation behavior close to the 2C-3C limit. On the contrary, the near-axis region between the two recirculation bubbles features an almost isotropic nature of the turbulence dissipation process. At the same time, downstream of the CRZ, a virtually two-component behavior arises. The same qualitative behavior characterizes Case 2, which is investigated in the right panel of Fig. 5(b). Even in this configuration, one principal direction dominates the turbulence dissipation tensor around the VB-induced stagnation point. In contrast, perfectly isotropic dissipation occurs along the jet evolution downstream of the stagnation point. The near-axis region of the CRZ shows vanishing levels of dissipation anisotropy. Concerning the recirculation bubble, two different behaviors are highlighted from the componentiality contour map: (i) the lower portion of the recirculation bubble, namely, between $z/R \approx 2$ and $z/R \approx 6$, especially in proximity of the ISL, features dissipation anisotropy states close to the axisymmetric expansion limit, similarly to what observed within the smaller recirculation bubble (B1) of Case 1; (ii) the upper portion of the recirculation bubble, i.e., up to $z/R \approx 9$, exhibits a dissipation behavior tending to the axisymmetric contraction limit, similarly to what observed within the larger recirculation bubble (B2) of Case 1. Therefore, it can be concluded that an almost opposite behavior in terms of anisotropic characteristics of the Reynolds stress and turbulence dissipation tensors arises under both bubble-type and regular conical VB conditions. As further discussed in Section 4.2.2, this provides meaningful information on how the dissipation tensor should be modeled in VB-affected swirling flows, in that Reynolds stress and small-scale anisotropies appear unrelated.

Further information about the componentiality of Reynolds stress and turbulence dissipation tensors can be gained by graphically visualizing ellipsoid-like glyphs, which are known to represent the shape of any second-order turbulence-related tensor (Simonsen and Krogstad, 2005). This visualization technique is illustrated in Figs. 6(a) and 6(b), which report the ellipsoid-like glyphs relative to the Reynolds stresses and dissipative turbulent scales, respectively. Consistently with Fig. 4(b), the lowest anisotropy degrees for the Reynolds stress tensor are envisaged within the initial portions of the ISL and OSL for both Case 1 and Case 2. On the contrary, one-component characteristics of the turbulent stresses affect the jet evolution region. From Fig. 6(b), it is again evident that the turbulence dissipation tensor retains a nearly three-component isotropic fashion along the main jet evolution and within the near-axis region of the CRZ, coherently with what shown in Fig. 5(b).

To further characterize the directional distribution of turbulence-related tensors, the axial distributions of the diagonal components of b_{ij} and d_{ij} are illustrated in Figs. 7 and 8.

In this respect, Fig. 7 highlights the fact that – under both swirling regimes – along the domain centerline, up to the VB-induced stagnation point, the axial velocity fluctuations entirely carry the turbulent kinetic energy budget, remarking the one-component nature of Reynolds stresses. Thereafter, at the bottom end of the CRZ, the flow field is virtually two-dimensional, with a vanishing axial velocity component. This results in an almost uniform distribution of the turbulent kinetic energy fractions amongst the radial and tangential components for Case 1 and Case 2. In contrast, the axial component does not contribute to any momentum exchange. This trend gradually varies beyond the smaller recirculation bubble for Case 1, with the axial component dominating the momentum exchange around $z/R \approx 4$. On the contrary, Reynolds stresses immediately revert to a one-component anisotropic behavior under Case 2 flow conditions. For both Case 1 and Case 2, a return-to-isotropy tendency arises at the upper end of the CRZ, namely, at $z/R \approx 6$ and $z/R \approx 10$, respectively. Nonetheless, further downstream, anisotropy levels increase again. On the other hand, the axial distribution of the diagonal elements of d_{ij} illustrated in Fig. 8

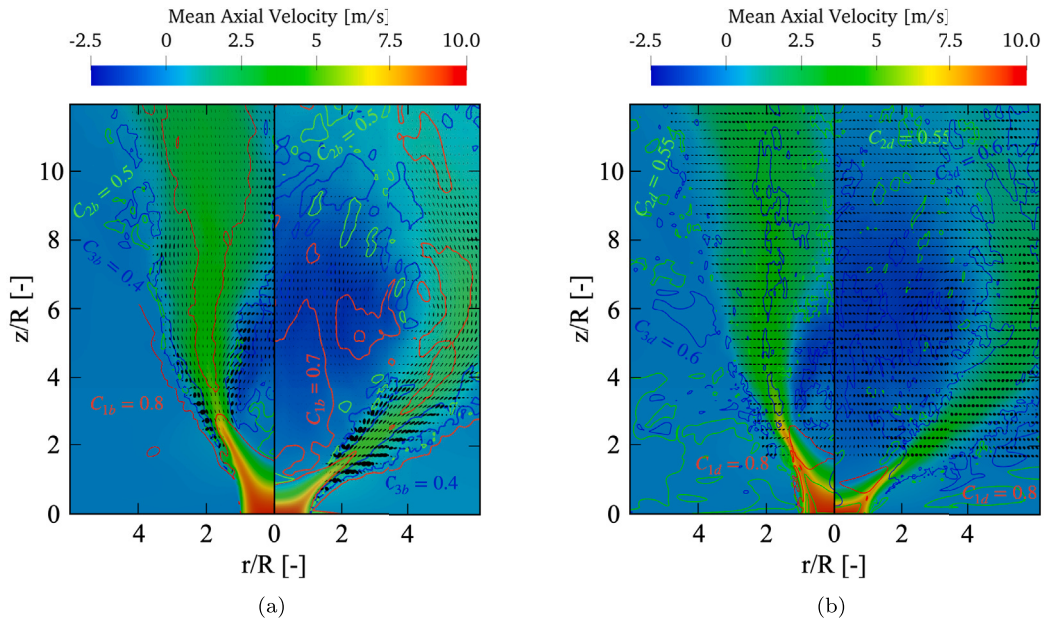

Fig. 6. Mean axial velocity field, overlapped with tensor characteristics in terms of ellipsoid-like glyphs for Case 1 (left) and Case 2 (right): (a) Reynolds stresses, (b) turbulence dissipation. Iso-lines of the barycentric weight coefficients (C_1, C_2, C_3) are shown in red, green, and blue, with b and d subscripts denoting Reynolds stresses and small-scale turbulent motions, respectively. (For interpretation of the references to color in this figure legend, the reader is referred to the web version of this article.)

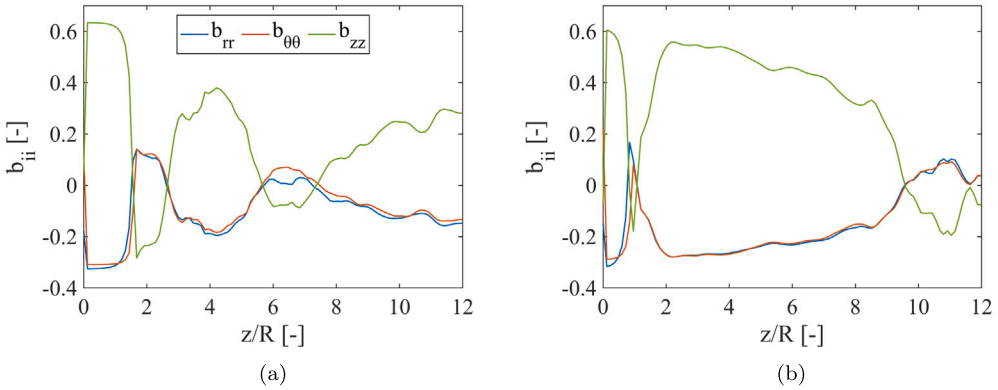

Fig. 7. Reynolds stress anisotropy tensor, axial distribution of diagonal components: (a) Case 1, (b) Case 2.

reveals that, in the whole stagnation region, turbulence dissipation occurs almost exclusively along the axial direction for both Case 1 and Case 2. Considerably lower anisotropy levels are envisaged within the near-axis region of the CRZ. Nonetheless, for Case 1, turbulence dissipation practically reverts to a two-component nature downstream of the CRZ, i.e., beyond $z/R \approx 6$, with the radial and tangential components carrying the most relevant fractions of the scalar dissipation rate. In contrast, this separation amongst the components of d_{ij} is less pronounced for Case 2.

Furthermore, Figs. 9 and 10 report the radial distribution of the diagonal components of b_{ij} and d_{ij} for Case 1 at three axial locations. Notably, Figs. 9(a) and 10(a) investigate the radial distribution at $z/R = 2.5$. While low anisotropy levels are evident for both $\langle u_i' u_j' \rangle$ and ϵ_{ij} in the proximity of the centerline, the anisotropy degree slightly increases within the smaller recirculation bubble (B1), as also pointed out by the inter-related oscillations of the diagonal components of both tensors. Thereafter, the main jet region - around $r/R \approx 1.5$ - features turbulent stresses and turbulence dissipation largely oriented along the axial and radial directions, respectively. On the contrary, a return-to-isotropy tendency for both tensors is envisaged in correspondence with the OSL, namely, at $r/R \approx 2$. At the same time, radial velocity fluctuations distinctly dominate the turbulent kinetic energy budget in the entrainment region, i.e., beyond $r/R \approx 2$. Figs. 9(b) and 10(b) show the radial evolution of Reynolds stress and small-scale anisotropy tensors at $z/R = 4$. For what concerns Reynolds stresses, axial velocity fluctuations carry the most relevant fraction of turbulent kinetic energy in the near-axis region. The main jet region - around $r/R \approx 2$ - is affected by turbulent stresses largely oriented along the axial direction, while an isotropic turbulence state is found within the OSL, i.e., at $r/R \approx 2.5$. Then, in the entrainment region, the radial velocity fluctuations still dominate. On the other hand, while turbulence dissipation is almost isotropic close to the domain centerline, an anisotropic state tending to two-component behavior is observed within the larger recirculation bubble (B2) and the main jet region, where d_{zz} barely contributes to the scalar dissipation rate of turbulent kinetic energy. At larger radial distances, the OSL exhibits a rapid return to isotropy within its outermost portion, i.e., at $r/R \approx 3.5$. Lastly, Figs. 9(c) and 10(c) illustrate the radial distribution of b_{ii} and d_{ii} at $z/R = 8$. While a vanishing anisotropy degree of the Reynolds stresses is envisaged at small radial distances, the evolution of Reynolds stress anisotropy in the main jet region and the OSL closely resembles the one already investigated at $z/R = 4$. Concerning the small-scale turbulent motions, a distinct two-component nature is observed close to the axis, with

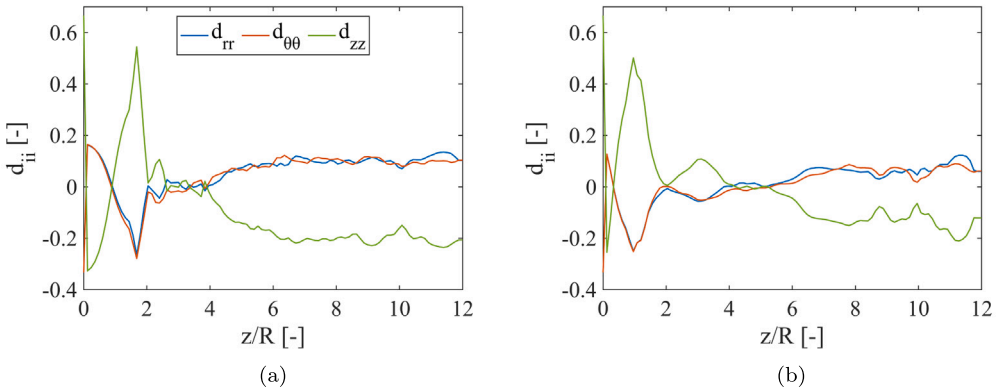

Fig. 8. Turbulence dissipation anisotropy tensor, axial distribution of diagonal components: (a) Case 1, (b) Case 2.

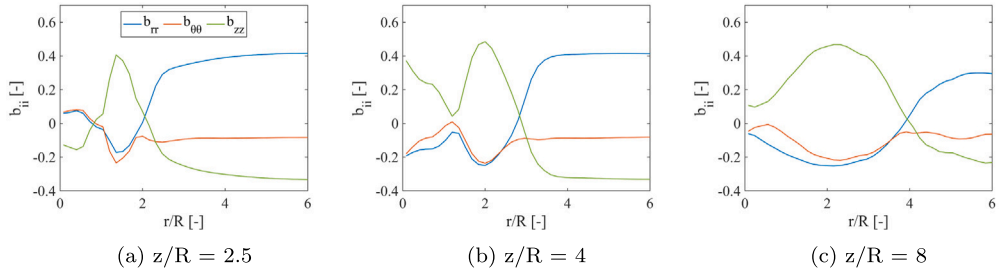

Fig. 9. Reynolds stress anisotropy tensor, radial distributions of diagonal components for Case 1: (a) z/R = 2.5, (b) z/R = 4, (c) z/R = 8.

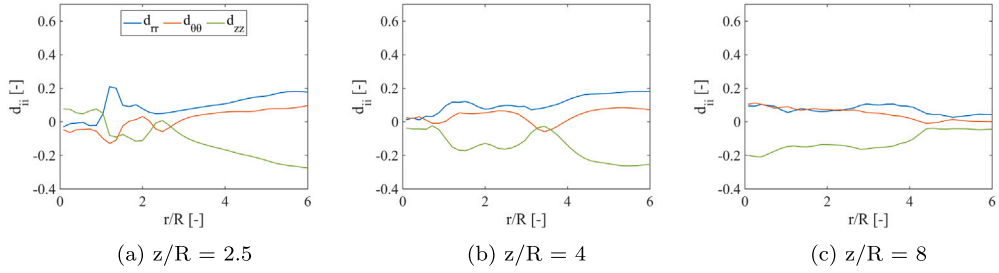

Fig. 10. Turbulence dissipation anisotropy tensor, radial distributions of diagonal components for Case 1: (a) z/R = 2.5, (b) z/R = 4, (c) z/R = 8.

turbulence dissipation largely oriented along the $r\theta$ plane. At larger radial distances, the anisotropy level gradually decreases, with the main jet region featuring largely isotropic dissipation characteristics.

Similarly, Figs. 11 and 12 report the radial distribution of the diagonal components of b_{ij} and d_{ij} for Case 2 at three axial locations. Precisely, Figs. 11(a) and 12(a) investigate the radial distribution at $z/R = 2$. Regarding Reynolds stresses, the axial velocity fluctuations mostly contribute to the turbulent kinetic energy budget inside the CRZ. At the same time, a pronounced return to isotropy can be envisaged in the ISL and OSL, i.e., at $r/R \approx 2$ and $r/R \approx 4$, respectively. Furthermore, the jet evolution region exhibits a departure from isotropy but, differently from what was observed for Case 1, there is no distinctly dominating fluctuation amongst the diagonal components of b_{ij}. Within the entrainment region, namely, beyond $r/R \approx 4.5$, the radial velocity fluctuations almost entirely carry the overall turbulent kinetic energy level. On the other hand, the turbulence dissipation process retains an almost isotropic behavior close to the domain centerline. Thereafter, d_{zz} largely increases against the other two components within the outermost portion of the CRZ. In contrast, the main jet region features a perfectly isotropic dissipation state. Figs. 11(b) and 12(b) show the radial evolution of Reynolds stress and small-scale anisotropy tensors at $z/R = 6$. Specifically, an almost one-component nature of the turbulent stresses is envisaged over the entire radial direction, with the axial velocity fluctuations providing a dominant contribution to the turbulent kinetic energy budget. The exception to this behavior is envisaged within the region close to the circumferential axis of the toroidal recirculation bubble, i.e., at $r/R \approx 3.75$, with a decrease in the anisotropy degree. In contrast, lower anisotropy levels characterize the turbulence dissipation process along the radial direction at $z/R = 6$. Lastly, Figs. 11(c) and 12(c) illustrate the radial distribution of b_{ii} and d_{ii} at $z/R = 10$. Concerning Reynolds stresses, anisotropic states close to the axisymmetric contraction limit can be envisaged up to $r/R \approx 3$, with a gradual shift toward the 3C isotropic limit. At larger radial distances, within the main jet region, the turbulence behavior starts exhibiting a one-component nature, with b_{zz} dominating the remaining two components. On the other hand, anisotropy levels of ϵ_{ij} are not pronounced. Still, the behavior of the anisotropy tensor components denotes how the turbulence dissipation along the axial direction gives a marginal contribution compared with d_{rr} and $d_{\theta\theta}$.

To summarize the key results about the fundamental characteristics of the turbulence dissipation tensor under VB flow conditions derived from the anisotropy analysis presented above, Fig. 13 provides three-dimensional visualization of coherent vortex structures induced by

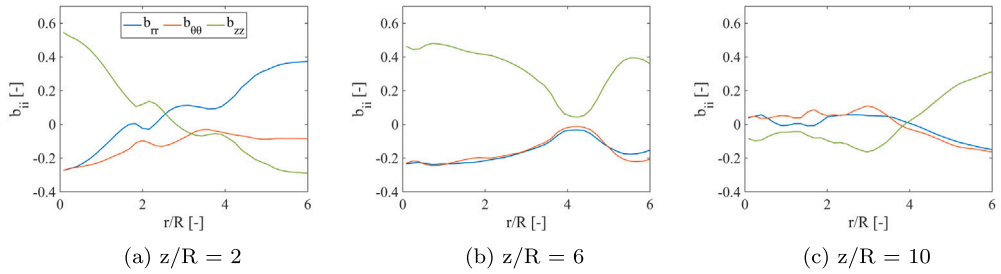

(a) z/R = 2 (b) z/R = 6 (c) z/R = 10

Fig. 11. Reynolds stress anisotropy tensor, radial distributions of diagonal components for Case 2: (a) z/R = 2, (b) z/R = 6, (c) z/R = 10.

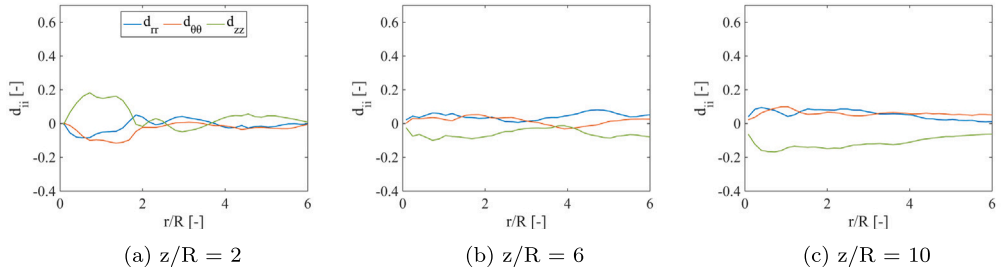

(a) z/R = 2 (b) z/R = 6 (c) z/R = 10

Fig. 12. Turbulence dissipation anisotropy tensor, radial distributions of diagonal components for Case 2: (a) z/R = 2, (b) z/R = 6, (c) z/R = 10.

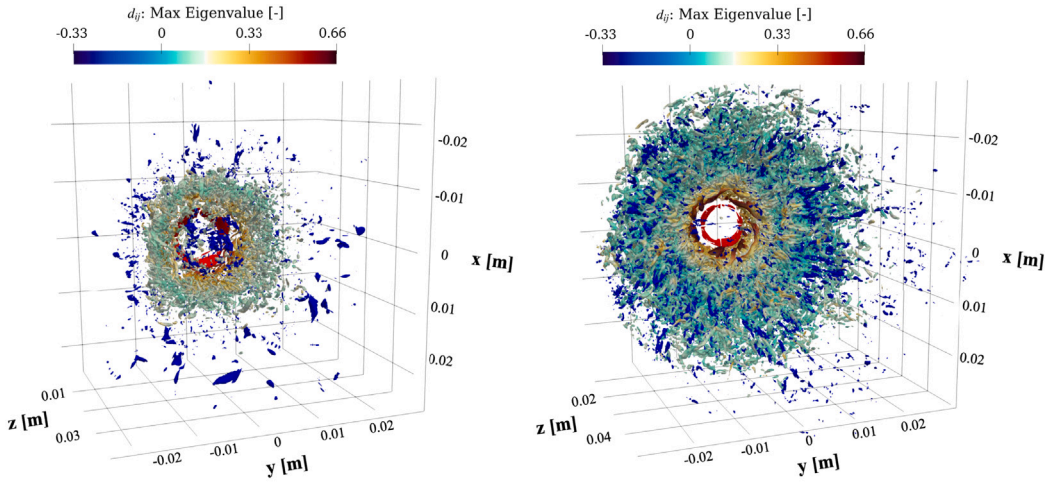

(a) Case 1 (b) Case 2

Fig. 13. Direct numerical simulation of vortex breakdown states: (a) Case 1, (b) Case 2. Coherent vortex structures are visualized employing Q-criterion isosurfaces, namely, $Q = 2.0 \times 10^7$ for Case 1 and $Q = 4.0 \times 10^6$ for Case 2, colored by the largest eigenvalue of the dissipation anisotropy tensor, d_{ij}. Iso-levels of $C_{1,d}$ and $C_{3,d}$ are shown in red and blue, respectively, namely $C_{1,d} = 0.99$ and $C_{3,d} = 0.8$ for Case 1, $C_{1,d} = 0.99$ and $C_{3,d} = 0.9$ for Case 2. (For interpretation of the references to color in this figure legend, the reader is referred to the web version of this article.)

breakdown phenomenology, along with relevant iso-level surfaces of weight coefficients $C_{1,d}$ and $C_{3,d}$ for the barycentric map relative to ϵ_{ij}. Indeed, those iso-contours provide valuable information on the topological distribution of one-component and perfectly isotropic turbulence dissipation behaviors. Notably, for both Case 1 and Case 2, one-component turbulence dissipation characteristics are exclusively concentrated around the VB-induced stagnation point, consistently with the componentiality contour maps shown in Fig. 5(b). Conversely, almost isotropic turbulence dissipation occurs in the proximity of the near-axis region inside the CRZ and within the jet evolution region.

4.2. Testing algebraic anisotropic dissipation tensor models

The anisotropy analysis carried out throughout Section 4.1 highlighted the distinctly one-component anisotropic nature of the Reynolds stress tensor in most regions of the flow configurations of interest, except for the lower and upper end of the CRZ and the shear layer zones. On the contrary, an essentially anisotropic behavior of the turbulence dissipation process is exclusively concentrated in specific flow field regions, which feature mostly isotropic Reynolds stresses, as remarked above. Hence, in the present Section, we first review existing anisotropic dissipation tensor models. Notably, given that non-algebraic models (Oberlack, 1997) - which derive the dissipation tensor from its transport equation - introduce complexity and model uncertainties, also considering the variety of arguments still unresolved concerning the modeling of other terms in Eq. (1) (Jakirlić and Hanjalić, 2002), we focus on algebraic models for the dissipation rate tensor. Thereafter, we test a set of these algebraic models against the reference DNS data, together with the standard isotropic formulation.

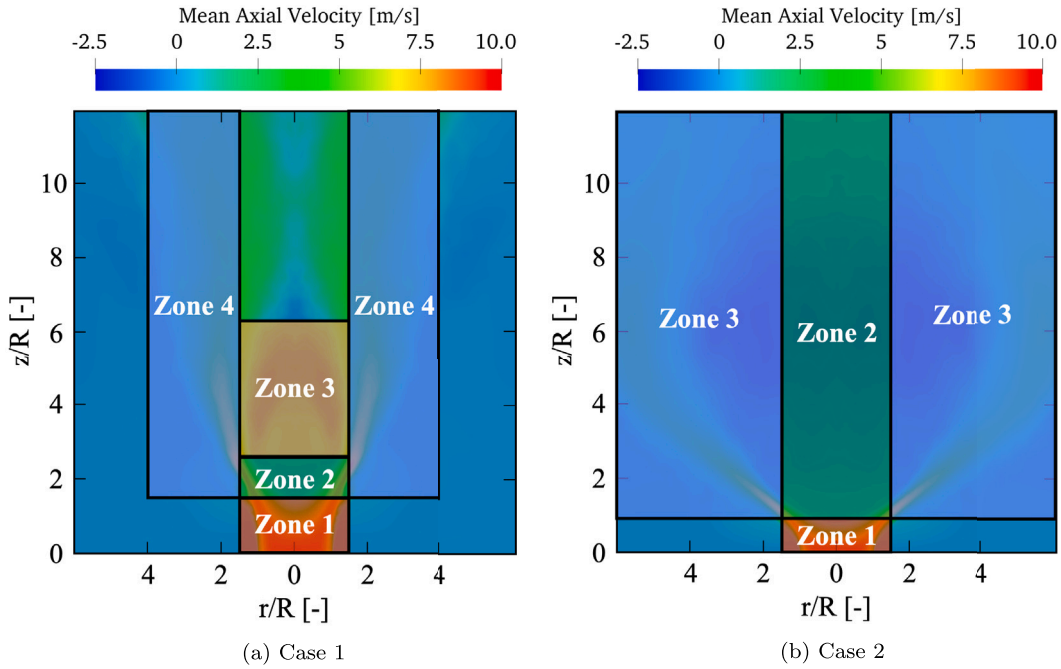

(a) Case 1 (b) Case 2

Fig. 14. Selected flow regions to investigate the discrepancy between DNS data and algebraic dissipation tensor formulations: (a) Case 1, (b) Case 2.

4.2.1. Review of algebraic models

The most straightforward anisotropic formulation was first proposed by Rotta (1951), $\varepsilon_{ij} = \frac{\varepsilon}{k}\langle u_i' u_j' \rangle$, directly implying that the Reynolds stress anisotropy equals the small-scale anisotropy, namely $b_{ij} = d_{ij}$. Several models (Hanjalić and Launder, 1976; Hallbäck et al., 1996) were proposed to combine the isotropic approach and Rotta's formulation through a blending parameter, f_s, which is typically a function of the turbulent Reynolds number, $Re_\tau = \frac{k^2}{\nu\varepsilon}$:

$$\varepsilon_{ij} = (1 - f_s)\frac{2}{3}\varepsilon\delta_{ij} + f_s\frac{\varepsilon}{k}\langle u_i' u_j' \rangle. \tag{10}$$

In this context, the model by Hanjalić and Launder (1976) uses $f_s = \frac{1}{1+0.1Re_\tau}$, while the model by Hallbäck et al. (1996) uses $f_s = \frac{1}{1+\frac{31}{5\pi}\frac{k^{0.5}L_f}{\nu}}$, with L_f denoting the integral length scale. In both cases, a linear relationship between d_{ij} and b_{ij}, i.e., $d_{ij} = f_s b_{ij}$, is returned. Additional models were developed (Sjögren and Johansson, 2000; Hallbäck et al., 1990) to characterize the small-scale anisotropy tensor, d_{ij}, as a function of the Reynolds stress anisotropy tensor, b_{ij}, ultimately providing:

$$\varepsilon_{ij} = \frac{2}{3}\varepsilon\delta_{ij} + f_{s,1}\varepsilon b_{ij} + f_{s,2}\varepsilon\left[b_{ik}b_{kj} - \frac{1}{3}b_{ij}b_{ji}\delta_{ij}\right]. \tag{11}$$

In particular, the linear model by Sjögren and Johansson (2000) uses $f_{s,1} = 1 - \frac{1}{2}\det\left[\frac{3\langle u_i' u_j' \rangle}{2k}\right]$ and $f_{s,2} = 0$. In contrast, the quadratic model by Hallbäck et al. (1990) uses $f_{s,1} = \frac{1}{2} + \frac{3}{8}b_{ij}b_{ji}$ and $f_{s,2} = -\frac{3}{4}$. On the other hand, starting from the exact transport equation for ε_{ij}, Speziale and Gatski (1997) developed an algebraic relation for d_{ij}, as a non-linear function of the mean velocity gradients for two-dimensional strain-dominated flows, which can also be applied to three-dimensional flows in principle. In this approach, mean velocity gradients should enhance different anisotropy characteristics in the Reynolds stresses and small-scale turbulent motions (So et al., 1999). The parameterization of ε_{ij} in terms of the mean flow gradients was also adopted by Perot and Natu (2004), resulting in an exact model in the proximity of solid walls or free surfaces, which can also be employed away from boundaries.

4.2.2. Performance of selected algebraic models

Along with the isotropic model derived from Kolmogorov's theory (Frisch, 1995), we investigate the performance of three different algebraic models for ε_{ij} against the available DNS datasets: (i) the model by Hallbäck et al. (1996), from now on designated as HJB; (ii) the model by Sjögren and Johansson (2000), from now on designated as SJ, which is linear in Reynolds stress anisotropies; (iii) the model by Hallbäck et al. (1990), from now on designated as HGJ, which is quadratic in Reynolds stress anisotropies. The formulations of ε_{ij} associated with these four models are summarized in Table 2.

To assess the performance of the models mentioned above, the discrepancy between DNS data and the algebraic dissipation tensor formulations is measured by resorting to the relative root mean square error ($RRMSE$) on the diagonal components of the turbulence dissipation tensor:

$$RRMSE(\%) = \frac{\sqrt{\frac{1}{3}\sum_{i=1}^{3}\left[\varepsilon_{ii}^{(\mathrm{DNS})} - \hat{\varepsilon}_{ii}\right]^2}}{\sum_{i=1}^{3}\varepsilon_{ii}^{(\mathrm{DNS})}} \cdot 100, \tag{12}$$

where $\varepsilon_{ii}^{(\mathrm{DNS})}$ and $\hat{\varepsilon}_{ii}$ are the diagonal components of the turbulence dissipation tensor returned by DNS computations and algebraic models, respectively.

Precisely, we focus on four specific flow regions for Case 1 and three specific flow regions for Case 2, as illustrated in Fig. 14.

Then, the discrepancy measure ultimately adopted is the $RRMSE$ conditioned on the fractional anisotropy of the dissipation tensor, FA_d, and averaged across the flow region of interest. In this regard, FA_d is defined as:

$$FA_d = \sqrt{\frac{1}{2}}\frac{\sqrt{(\tilde{\lambda}_1 - \tilde{\lambda}_2)^2 + (\tilde{\lambda}_2 - \tilde{\lambda}_3)^2 + (\tilde{\lambda}_3 - \tilde{\lambda}_1)^2}}{\sqrt{\tilde{\lambda}_1^2 + \tilde{\lambda}_2^2 + \tilde{\lambda}_3^2}}, \tag{13}$$

with $\tilde{\lambda} = (\tilde{\lambda}_1, \tilde{\lambda}_2, \tilde{\lambda}_3)$ denoting the eigenvalues of $\varepsilon_{ij}^{(\mathrm{DNS})}$ in descending order. Furthermore, the conditional PDF of $RRMSE$, given the value $\overline{FA}_d$ taken by FA_d, may be expressed as:

$$f_{RRMSE|FA_d}(\overline{RRMSE} \mid \overline{FA}_d) = \frac{f_{RRMSE,FA_d}(\overline{RRMSE}, \overline{FA}_d)}{f_{FA_d}(\overline{FA}_d)}, \tag{14}$$

Table 2
Collection of algebraic dissipation tensor models tested against DNS data.

Name	Model	Ref.
Isotropic	$\varepsilon_{ij} = \frac{2}{3}\varepsilon\delta_{ij}$	Frisch (1995)
HJB	$\varepsilon_{ij} = (1-f_s)\frac{2}{3}\varepsilon\delta_{ij} + f_s\frac{\varepsilon}{k}\langle u_i'u_j'\rangle$ with $f_s = \left[1+\frac{31}{5\pi}\frac{k^{0.5}L_f}{\nu}\right]^{-1}$	Hallbäck et al. (1996)
SJ	$\varepsilon_{ij} = \frac{2}{3}\varepsilon\delta_{ij} + f_{s,1}\varepsilon b_{ij}$ with $f_{s,1} = 1-\frac{1}{2}\det\left[3\langle u_i'u_j'\rangle/2k\right]$	Sjögren and Johansson (2000)
HGJ	$\varepsilon_{ij} = \frac{2}{3}\varepsilon\delta_{ij} + f_{s,1}\varepsilon b_{ij} - \frac{3}{4}\varepsilon\left[b_{ik}b_{kj} - \frac{1}{3}b_{ij}b_{ji}\delta_{ij}\right]$ with $f_{s,1} = \frac{1}{2}+\frac{3}{8}b_{ij}b_{ji}$	Hallbäck et al. (1990)

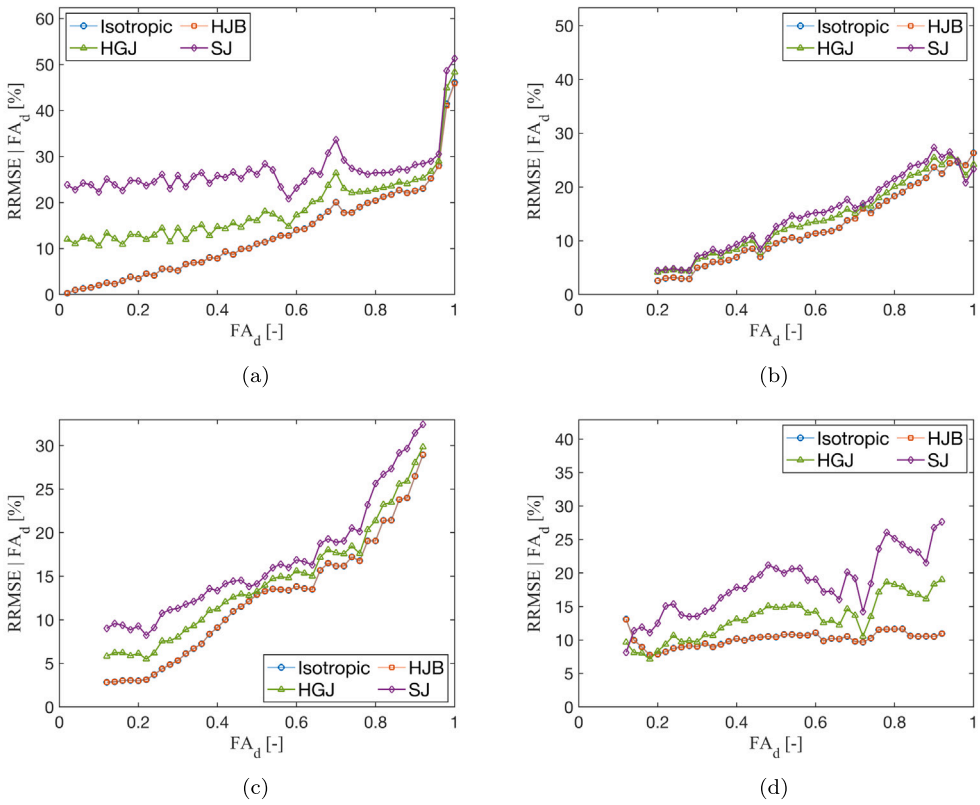

Fig. 15. Conditional average error on the diagonal components of the turbulence dissipation tensor, ε_{ij}, as a function of the small-scale fractional anisotropy, FA_d, for Case 1: (a) Zone 1, (b) Zone 2, (c) Zone 3, (d) Zone 4.

where $f_{RRMSE,FA_d}(\overline{RRMSE}, \overline{FA}_d)$ denotes the joint density of $RRMSE$ and FA_d, whereas $f_{FA_d}(\overline{FA}_d)$ indicates the marginal density of FA_d.

Fig. 15 illustrates the average $RRMSE$ conditioned on FA_d within the four different flow regions for Case 1. Precisely, Zone 1 corresponds to the jet region up to the VB-induced stagnation point. As shown in Fig. 15(a), the isotropic and HJB models are perfectly overlapped and present an increasing trend with FA_d. The SJ and HGJ models constantly return higher conditional errors than the other models, providing 10% and 25% error values, respectively, even at vanishing anisotropy levels. Thereafter, within Zone 2 - placed at the bottom of the CRZ - an increasing trend with FA_d is still shown in Fig. 15(b). However, disparities between the four models are minimal. In particular, while the isotropic and HJB models, still overlapped, exhibit a similar discrepancy against DNS data compared with Zone 1, the SJ and HGJ models show improved performance. Moreover, the average conditional errors returned by any model at extremely anisotropic levels, i.e., $FA_d \approx 1$, are lower compared with Zone 1. Similar considerations apply to Zone 3, which corresponds to the CRZ, and Zone 4, which encompasses both the main jet region and shear layer zones, see Figs. 15(c) and 15(d), respectively. Even in these cases, the isotropic and HJB models virtually coincide, whereas the SJ and HGJ models always provide higher conditional error levels. Moreover, the FA_d values investigated in Zone 3 and Zone 4 keep below 1, reaffirming that the maximum anisotropy degree of the dissipation tensor can be found around the VB-induced stagnation point.

Fig. 16 illustrates the average $RRMSE$ conditioned on FA_d within the three different flow regions for Case 2. It is worth highlighting from the beginning that the isotropic and HJB models also perfectly overlap under conical VB conditions, regardless of the flow zone under consideration. Again, Zone 1 corresponds to the jet region upstream of the VB-induced stagnation point, and Fig. 16(a) provides consistent results compared with Zone 1 of Case 1. Thereafter, within Zone 2 - which spans the stagnation region and the innermost portion of the CRZ - the SJ and HGJ models only return error levels comparable with the remaining models from $FA_d = 0.7$ on, as reported in Fig. 16(b). This trend is confirmed in Zone 3, which encompasses the outermost portion of the CRZ, the main jet region, and the shear layer. Nonetheless, the models involving a relation between ε_{ij} and b_{ij}, namely, the SJ and HGJ models, provide slightly lower discrepancies with the DNS data beyond $FA_d \approx 0.8$.

Therefore, the model comparison carried out for both Case 1 and Case 2 shows an overall superiority of the isotropic and HJB models compared with the SJ and HGJ formulations, which involve a linear and quadratic relation between the dissipation tensor and the Reynolds stress anisotropies, respectively. Nonetheless, the performance of the former two models still deteriorates with increasing anisotropy level in ε_{ij}, returning average conditional errors up to 50% around the

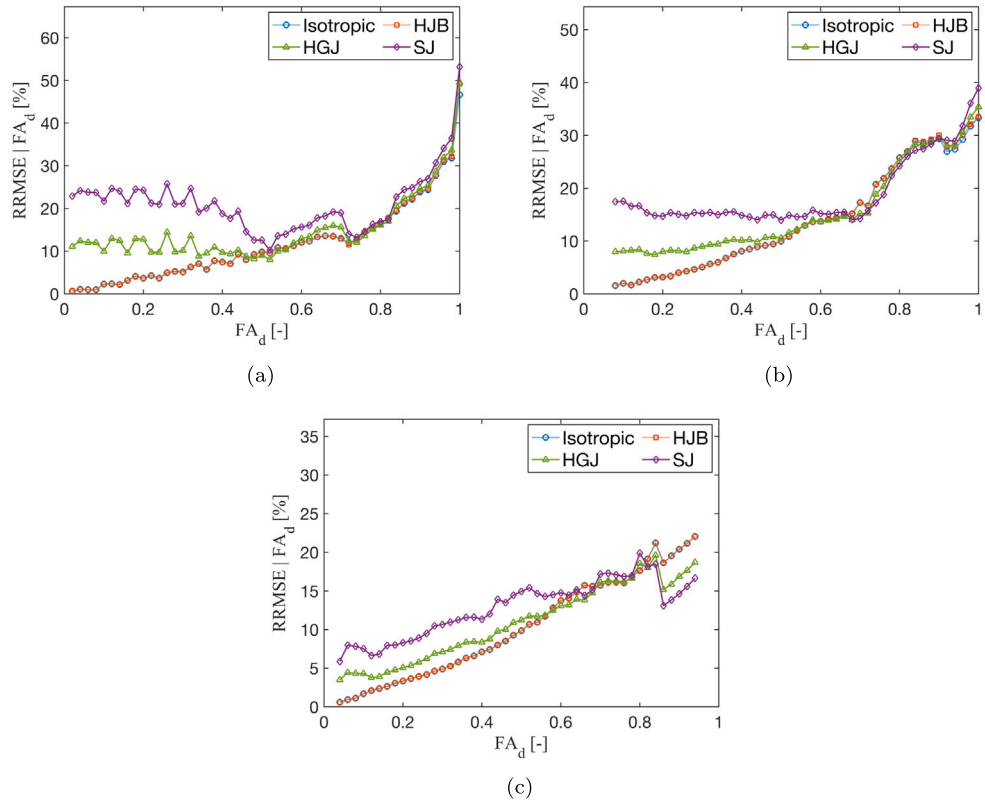

Fig. 16. Conditional average error on the diagonal components of the turbulence dissipation tensor, ϵ_{ij}, as a function of the small-scale fractional anisotropy, FA_d, for Case 2: (a) Zone 1, (b) Zone 2, (c) Zone 3.

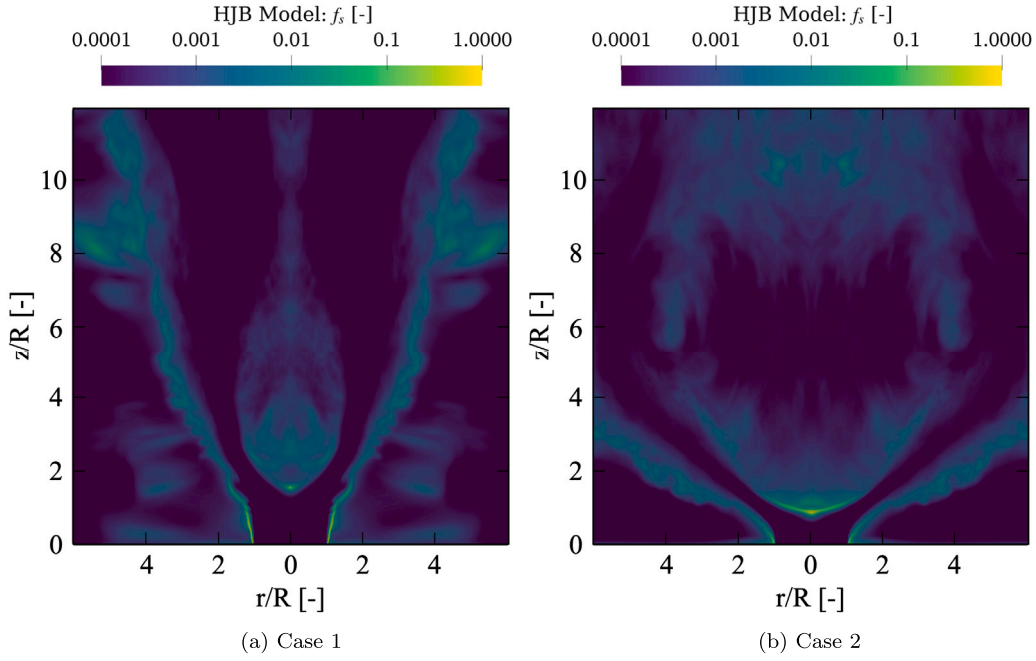

Fig. 17. Mean distribution of the HJB blending coefficient, f_s: (a) Case 1, (b) Case 2. Note that a logarithmic scale is used.

stagnation point established due to the breakdown phenomenology. Hence, improved modeling of the turbulence dissipation tensor via algebraic models for moderately to highly swirling flows undergoing VB should still be pursued. Specifically, as demonstrated concerning the SJ and HGJ models, merely relating dissipation anisotropy characteristics to the anisotropy of the Reynolds stresses, i.e., b_{ij}, is not sufficient to capture the anisotropic nature of ϵ_{ij} in specific regions of VB-affected jets. Consequently, the formulation of ad-hoc algebraic dissipation tensor models should eventually include additional flow field features, e.g., the mean velocity gradients (Speziale and Gatski, 1997; So et al., 1999; Perot and Natu, 2004), which will be the focus of future research work.

Lastly, Fig. 17 illustrates the mean spatial distribution of the HJB model blending coefficient, f_s, for Cases 1 and 2. Under both VB regimes, the blending coefficient takes vanishing values in the main jet region and the middle area of the CRZ, causing the HJB model to revert to the standard isotropic formulation where the dissipation tensor is expected to experience an almost isotropic behavior, see Fig. 5(b). On the contrary, non-vanishing values of f_s can be envisaged within the shear layer zones, around the VB-induced stagnation point and at the upper end of the CRZ, thus reflecting the tendency of the HJB model to tend toward the anisotropic Rotta's model in those regions where a remarkable departure from isotropy is observed concerning ε_{ij}, as shown in Fig. 5(b). Therefore, formulating an algebraic dissipation tensor model based on a blending between an isotropic and an anisotropic approach regulated by the turbulent Reynolds number looks promising. Still, the values taken by f_s in the HJB model barely tend to unity, resulting in a model closely resembling the standard isotropic formulation. Therefore, although the development of such a blending approach appears to correctly identify those flow regions where an anisotropic treatment of the dissipation tensor is necessary, further improvement about the definition - and consequently the magnitude - of f_s should be pursued, along with ad-hoc formulations of the anisotropic contribution to replace the basic model by Rotta, eventually including mean local flow field properties, as stated above.

5. Summary and conclusions

In the present work, we investigated two swirling jets undergoing bubble-type and regular conical vortex breakdown via direct numerical simulation. We exploited this high-fidelity database to analyze the anisotropic characteristics of the Reynolds stress and turbulence dissipation tensors. By resorting to componentiality contours derived from the standard anisotropy maps, namely, the Lumley triangle and the barycentric map, the anisotropy analysis revealed that: (i) Reynolds stresses exhibit a one-component anisotropic behavior in most flow regions under both vortex breakdown regimes, except for the inner and outer shear layer regions, and the bottom and top extremities of the breakdown-related central recirculation zone; (ii) the dissipation tensor features a less significant departure from isotropy, yet, remarkable anisotropic states are found where the Reynolds stresses experience a return-to-isotropy tendency, especially in the proximity of the breakdown-induced stagnation point. Based on the outcome of the anisotropy analysis, suggesting that ad-hoc modeling of the dissipation tensor is, in principle, necessary under vortex breakdown conditions, we tested the standard isotropic model and three algebraic anisotropic dissipation tensor formulations against the reference data: (i) the HJB model, combining the isotropic treatment with the basic anisotropic formulation proposed by Rotta through a turbulent-Reynolds-number-dependent blending function; (ii) the SJ model, combining the isotropic treatment with a linear expression in the Reynolds stress anisotropy tensor; (iii) the HGJ model, combining the isotropic treatment with a quadratic expression in the Reynolds stress anisotropy tensor. On the one hand, the blending function of the HJB model exhibited the capability of identifying the flow regions where mostly anisotropic turbulence dissipation occurs. However, due to the current formulation, the HJB model generally reverts to the basic isotropic approach. On the other hand, the SJ and HJB models showed worse agreement with the direct numerical simulation data, proving that exclusively relating small-scale anisotropies to Reynolds stress anisotropic behavior is unsuitable for breakdown-affected swirling flows. Hence, the outcome of the present research study suggests that ad-hoc treatment of the turbulence dissipation tensor in swirling flows undergoing vortex breakdown should target an enhancement of currently available blended formulations regulated by the turbulent Reynolds number, improving the blending function definition and including mean local flow properties within the anisotropic contribution of the model.

CRediT authorship contribution statement

Jacopo Liberatori: Writing – original draft, Methodology, Investigation, Conceptualization. **Mauro Valorani:** Writing – review & editing, Supervision. **Pietro Paolo Ciottoli:** Writing – review & editing, Supervision.

Declaration of competing interest

The authors declare that they have no known competing financial interests or personal relationships that could have appeared to influence the work reported in this paper.

Data availability

Data will be made available on request.

References

Antonia, R.A., Djenidi, L., Spalart, P.R., 1994. Anisotropy of the dissipation tensor in a turbulent boundary layer. Phys. Fluids 6, 2475–2479.

Banerjee, S., Krahl, R., Durst, F., et al., 2007. Presentation of anisotropy properties of turbulence, invariants versus eigenvalue approaches. J. Turbul. 8, N32.

Blandino, M., Liberatori, J., Cavalieri, D., et al., 2024. Turbulence closure assessment in URANS of a cold-flow lab-scale swirled burner. In: 2024 AIAA Science and Technology Forum and Exposition.

Choi, J., Do, H., 2018. Modeling swirl decay rate of turbulent flows in annular swirl injectors. AIAA J. 56 (12), 4910–4926.

Ciottoli, P.P., Battista, F., Malpica Galassi, R., et al., 2021. Direct numerical simulations of the evaporation of dilute sprays in turbulent swirling jets. Flow Turbul. Combust. 106, 993–1015.

Dalla Barba, F., Picano, F., 2018. Clustering and entrainment effects on the evaporation of dilute droplets in a turbulent jet. Phys. Rev. Fluids 3, 034304.

Durbin, P., Speziale, C.G., 1991. Local anisotropy in strained turbulence at high Reynolds number. J. Fluids Eng. Trans. ASME 113, 707–709.

Emory, M., Iaccarino, G., 2014. Visualizing turbulence anisotropy in the spatial domain with componentality contours. In: Center for Turbulence Research, Annual Research Briefs. pp. 123–138.

Frisch, U., 1995. The kolmogorov 1941 theory. In: Turbulence: The Legacy of A.N. Kolmogorov. Cambridge University Press, pp. 72–99.

Gerolymos, G.A., Vallet, I., 2016. The dissipation tensor ε_{ij} in wall turbulence. J. Fluid Mech. 807, 386–418.

Hallbäck, M., Groth, J., Johansson, A.V., 1990. An algebraic model for nonisotropic turbulent dissipation rate in Reynolds stress closures. Phys. Fluids A: Fluid Dyn. 2, 1859–1866.

Hallbäck, M., Johansson, A.V., Burden, A.D., 1996. The basics of turbulence modeling. In: Turbulence and Transition Modeling. In: Lecture notes from the ERCOFTAC/IUTAM Summer School in Stockholm 12-20 June, 2, Chap. 3, ERCOFTAC series, Kluwer, Dordrecht.

Hanjalić, K., Launder, B.E., 1976. Contribution towards a Reynolds-stress closure for low-Reynolds-number turbulence. J. Fluid Mech. 74, 593–610.

Jakirlić, S., Hanjalić, K., 2002. A new approach to modelling near-wall turbulence energy and stress dissipation. J. Fluid Mech. 459, 139–166.

Jalalatian, N., Tabejamaat, S., Kashir, B., et al., 2019. An experimental study on the effect of swirl number on pollutant formation in propane bluff-body stabilized swirl diffusion flames. Phys. Fluids 31, 055105.

Lai, Y.G., So, R.M.C., 1990. On near-wall turbulent flow modelling. J. Fluid Mech. 221, 641–673.

Launder, B.E., Li, B.L., 1994. On the elimination of wall topography parameters from second moment closure. Phys. Fluids 6, 999–1006.

Launder, B.E., Reece, G.J., Rodi, W., 1975. Progress in the development of a Reynolds-stress turbulence closure. J. Fluid Mech. 68, 537–566.

Liberatori, J., Battista, F., Dalla Barba, F., et al., 2024. Direct numerical simulation of vortex breakdown in evaporating dilute sprays. Flow Turbul. Combust. 112, 643–667.

Liberatori, J., Malpica Galassi, R., Valorani, M., et al., 2023. Uncertainty quantification analysis of Reynolds-averaged Navier–Stokes simulation of spray swirling jets undergoing vortex breakdown. Int. J. Spray Combust. Dyn. 15 (4), 218–236.

Liu, K., Pletcher, R.H., 2008. Anisotropy of a turbulent boundary layer. J. Turbul. 9, N18.

Lucca-Negro, O., O'Doherty, T., 2001. Vortex breakdown: A review. Prog. Energy Combust. Sci. 27 (4), 431–481.

Lumley, J.L., Newman, G., 1977. The return to isotropy of homogeneous turbulence. J. Fluid Mech. 82, 161–178.

Meunier, P., Hourigan, K., 2013. Mixing in a vortex breakdown flow. J. Fluid Mech. 731, 195–222.

Oberlack, M., 1997. Non-isotropic dissipation in non-homogeneous turbulence. J. Fluid Mech. 350, 351–374.
Oberleithner, K., Sieber, M., Nayeri, C.N., et al., 2011. Three-dimensional coherent structures in a swirling jet undergoing vortex breakdown: stability analysis and empirical mode construction. J. Fluid Mech. 679, 383–414.
Perot, B., Natu, S., 2004. A model for the dissipation rate tensor in inhomogeneous and anisotropic turbulence. Phys. Fluids 16, 4053.
Pope, S.B., 2000. Reynolds-stress and related models. In: Turbulent Flows. Cambridge University Press, pp. 387–462.
Rotta, J., 1951. Stastische theorie nichthomegener turbulenz I. Z. Phys. 129, 547–572.
Ruith, M.R., Chen, P., Meiburg, E., 2004. Development of boundary conditions for direct numerical simulations of three-dimensional vortex breakdown phenomena in semi-infinite domains. Comput. & Fluids 33 (9), 1225–1250.
Saddoughi, S.G., Veeravalli, S.V., 1994. Local isotropy in turbulent boundary layers at high Reynolds number. J. Fluid Mech. 268, 333–372.
Shen, X., Warhaft, Z., 2000. The anisotropy of the small scale structure in high Reynolds number ($Re_\lambda \sim 1000$) turbulent shear flow. Phys. Fluids 12, 2976–2989.
Simonsen, A.J., Krogstad, P.A., 2005. Turbulent stress invariant analysis: clarification of existing terminology. Phys. Fluids 17, 088103.
Sjögren, T., Johansson, A.V., 2000. Development and calibration of algebraic non-linear models for terms in the Reynolds stress transport equation. Phys. Fluids 12, 1554–1572.
Smyth, W.D., Moum, J.N., 2000. Anisotropy of turbulence in stably stratified mixing layers. Phys. Fluids 12, 1343–1362.
So, R.M.C., Zhao, C.Y., Gatski, T.B., 1999. Predicting buoyant shear flows using anisotropic dissipation rate models. Flow Turbul. Combust. 63, 193–221.
Speziale, C.G., Gatski, T.B., 1997. Analysis and modelling of anisotropies in the dissipation rate of turbulence. J. Fluid Mech. 344, 155–180.
Speziale, C.G., Sarkar, S., Gatski, T.B., 1991. Modelling the pressure-strain correlation of turbulence. An invariant dynamical systems approach. J. Fluid Mech. 227, 245–272.
Syred, N., Beér, J.M., 1974. Combustion in swirling flows: A review. Combust. Flame 23 (2), 143–201.
Yan, H., Liu, Y., Lu, L., 2019. Turbulence anisotropy analysis in a highly loaded linear compressor cascade. Aerosp. Sci. Technol. 91, 241–254.
Yang, X., Gui, N., Xie, G., et al., 2015. Anisotropic characteristics of turbulence dissipation in swirling flow: A direct numerical simulation study. Adv. Math. Phys. 2015, 657620.
Yeung, P., Brasseur, J., 1991. The response of isotropic turbulence to isotropic and anisotropic forcing at the large scales. Phys. Fluids A 3, 884–897.
Yeung, P., Brasseur, J., Wang, Q., 1995. Dynamics of direct large-small scale couplings in coherently forced turbulence: Concurrent physical- and Fourier-space views. J. Fluid Mech. 283, 43–95.